Drivers of cold frontal hourly extreme precipitation: a climatological study over Europe

Article

Published Version

It is advisable to refer to the publisher's version if you intend to cite from the work. See Guidance on citing.

www.reading.ac.uk/centaur

CentAUR

Central Archive at the University of Reading

Reading's research outputs online

Drivers of Cold Frontal Hourly Extreme Precipitation: A Climatological Study Over Europe

Armin Schaffer[1] ⓘ, Tobias Lichtenegger[1] ⓘ, Heimo Truhetz[1] ⓘ, Albert Ossó[1] ⓘ, Oscar Martínez-Alvarado[2,3] ⓘ, and Douglas Maraun[1] ⓘ

[1]Wegener Center for Climate and Global Change, University of Graz, Graz, Austria, [2]Department of Meteorology, University of Reading, Reading, UK, [3]National Centre for Atmospheric Science, University of Reading, Reading, UK

Abstract In the mid-latitudes extreme precipitation events are strongly associated with cold fronts. By exploring drivers across different scales and relating them to precipitation, we aim to improve our understanding of processes influencing cold frontal extremes. Using hourly ERA5 data over Europe and the North Atlantic, cold fronts are detected and the associated conditions are identified. Quantile regression models are employed to find drivers of frontal precipitation and to quantify these relations. Additionally, we use composites to study the synoptic conditions and meso-scale structure of extreme events. We find that humidity close to the detected fronts, convergence and the low level jet speed contribute most to the formation of extreme precipitation. Synoptic conditions favoring the formation of extreme events are also identified. These results improve our understanding of cold frontal processes leading to precipitation. Additionally, they provide the foundation for a process-based evaluation of frontal dynamics in climate models.

Plain Language Summary Extreme rain, snow and hail events in the mid-latitudes are often caused by atmospheric cold fronts. To understand what makes certain events extreme, we need to study the processes and conditions influencing these fronts. In this study, we analyze the characteristics of cold fronts and their connection to extreme rain. First, we identify fronts in the ERA5 climate reanalysis data by finding strong changes in temperature and humidity over Europe and the North Atlantic. Next, we examine the conditions near these fronts. Using statistical models, we link these conditions to rain intensities. Additionally, the large-scale weather patterns are studied by looking at the average conditions. We find that atmospheric moisture content and the strength of certain frontal circulation patterns play the biggest role in creating extreme weather. These results help us to better understand cold fronts and provide the basis for evaluating frontal conditions in climate models.

1. Introduction

Extreme weather like windstorms, hail, and intense precipitation pose a threat to human life and property. In the mid-latitudes these impacts are frequently related to synoptic-scale atmospheric fronts. On average, 68% of annual precipitation in the mid-latitudes is related to fronts (Catto et al., 2012). The most intense short-term precipitation is commonly related to cold fronts, which can lead to flooding and other large damages, amplified by co-occurring squalls. Catto and Pfahl (2013) highlights that up to 40% of all extreme precipitation events in Europe can be attributed to cold fronts, underscoring the critical importance of understanding the mechanisms of these weather phenomena.

The processes related to the formation of extreme frontal precipitation are not well understood, contributing to uncertainties in forecasts and projections. Especially in sight of global warming, it is important to gain knowledge about the dynamic processes of mid-latitude weather systems which contribute to these uncertainties (Collins et al., 2018; Marotzke et al., 2017). Thus, the characteristics of fronts and the governing processes need to be studied to understand how these extremes form and might change due to rising temperatures.

Synoptic fronts are strongly related to cyclones and thus affected by large-scale processes (Hoskins & James, 2014). Synoptic air streams introduce convergence and transport humidity into frontal regions. Research into cold frontal precipitation showed an increase in precipitation with the presence of synoptic air streams for example, the warm conveyor belt (Catto et al., 2015) and the dry intrusion (Catto & Raveh-Rubin, 2019; Raveh-Rubin & Catto, 2019). However, meso-scale processes particularly influence the dynamic conditions within

Writing – review & editing:
Armin Schaffer, Tobias Lichtenegger,
Heimo Truhetz, Albert Ossó,
Oscar Martínez-Alvarado,
Douglas Maraun

frontal regions, shaping the weather associated with these fronts (Eliassen, 1962; Sawyer, 1956). Thus, to understand extremes, we need to study the interactions between synoptic-scale and frontal-scale processes.

Research into the impact of climate change on fronts is important for understanding future changes in extreme weather in the mid-latitudes. Fronts with extremely strong thermal gradients, which are related to more intense precipitation, have become more frequent over Europe (Schemm et al., 2017). On a regional level, precipitation related to fronts has decreased in some areas, possibly due to the displacement of the storm track further north (Hénin et al., 2019), while a study of front frequency changes in CMIP5 models indicates a decrease in front activity over northern and southern Europe (Catto et al., 2014).

Clark and Parker (2020) studied the impact of certain front characteristics on the likelihood of tornadogenesis in the United Kingdom and Ireland. A similar approach looking into the relation of front characteristics on precipitation has not been performed.

The aim of this study is to evaluate the characteristics of cold fronts and investigate their relation with extreme precipitation over Europe and the North Atlantic. A special focus is set on analyzing the dynamic processes of the synoptic- and meso-scale affecting fronts.

2. Data and Methods

We use the European Center for Medium-range Weather Forecast (ECMWF) reanalysis ERA5 dataset with 1 hr and 0.25° resolution (Hersbach et al., 2020). This resolution enables us to study meso-scale processes close to the frontal zone. However, relevant meso-γ scale processes are not resolved (Lin, 2007). Narrow cold frontal precipitation bands are ~5 km wide, with embedded small ellipsoid heavy precipitating areas (Houze & Hobbs, 1982). Thus, the fine scale structure of the precipitating areas is not resolved. The study region extends from 60°W–40°E to 30°N–75°N, encompassing large parts of Europe and the North Atlantic. We consider the period from 1940 to 2021 and perform all analyses for each season separately.

2.1. Front Detection

Following earlier studies (e.g., Hénin et al., 2019; Rüdisühli et al., 2020; Schemm et al., 2017), we detected fronts by applying a threshold to the equivalent potential temperature gradient ($\nabla\theta_e$) at 850 hPa. Due to the substantial seasonality of the specific humidity gradient, season-dependent thresholds are applied. The thresholds are 4.6, 4.9, 6.3, and 5.9 K·[100 km]$^{-1}$ for DJF, MAM, JJA, and SON, respectively. These values correspond to one standard score unit of the $\nabla\theta_e$ over the North Atlantic (50°W–12°W, 30°N–58°N) from 1979 to 2021 for each season.

First, the θ_e field is smoothed with a spectral filter. The spectral transformation is performed using the discrete cosine transformation (DCT) with a subsequent low-pass filtering (Denis et al., 2002). The filter preserves wavelengths larger than 1,000 km and transforms smaller wavelengths with a two-dimensional spectral Gaussian transfer function with its mean at 1,000 km and a standard deviation of 75 km (Figure S1 in Supporting Information S1). This procedure removes small-scale gradients and smooths the detected frontal regions, resulting in more coherent fronts while preserving their structure (Figure S2 in Supporting Information S1).

Frontal lines are then derived by utilizing the thermal front parameter (TFP) (Renard & Clarke, 1965). Following Ritter (2014), fronts are located at the TFP field zero contour within the frontal region. Thus, fronts are located at the maximum of $\nabla\theta_e$. The front advection speed is estimated by computing the smoothed 850 hPa wind along the TFP gradient, representing the cross-frontal direction. Front points are then classified into cold (positive cross-frontal wind speed) and warm fronts (negative cross-frontal wind speed) (e.g., Hénin et al., 2019; Hewson, 1998; Jenkner et al., 2009; Rüdisühli et al., 2020). A minimal cross-frontal wind speed of 1.5 m·s^{-1} is introduced, ensuring only mobile fronts are detected.

To evaluate the size of a front, neighboring detected frontal pixels are grouped into continuous front objects. Their length is then approximated by measuring the largest diagonal distance of the smallest box enclosing the front. Small fronts are removed by applying a size criterion of 500 km. In a final step, cold fronts are filtered by computing the difference between the $\nabla\theta_e$ and geopotential gradient angles. Frontal points with an absolute angle difference larger than 120° are excluded from the cold front analysis. These points are linked to back-bend occlusions, as well as humidity fronts following frontal passing at long coastal mountain ranges for example, the

Scandinavian Mountains and the Dinaric Alps. The front frequencies without this filter are displayed in Figure S3 in Supporting Information S1.

2.2. Front Parameters

To assess the characteristics of the fronts, we introduce parameters quantifying the thermodynamic and dynamic properties near them. This is done by evaluating the parameter fields in the cross-frontal direction at 0, 100, 200, and 300 km ahead and behind the front. A similar approach has been used by Clark and Parker (2020).

The amount of frontal precipitation is evaluated by computing the 90th percentile of the precipitation field within a radius of 150 km of each frontal point. These values are chosen to evaluate the regions of highest precipitation of cold fronts. An illustration of the parameter evaluation is given in Figure S4 in Supporting Information S1.

In this study, frontal precipitation intensity is quantified by 1 hr precipitation (average $\pm$1 hr accumulated precipitation), as well as the standardized 1 hr precipitation with respect to the seasonal climatology of each grid point. Atmospheric specific humidity, potential temperature (θ), θ_e, as well as gradients of these properties and the cross- and along-front wind speed are chosen as properties to quantify the characteristics of the fronts. These parameters are evaluated at the front detection height of 850 hPa. The dynamic fields are further split into the synoptic- and meso-scale using the spectral filter used in the front detection, similar to the approach presented by Feser and von Storch (2005). The filter settings are 1,500 km low pass and 500 km standard deviation of the transfer function (Figure S1 in Supporting Information S1), ensuring wavelengths larger than 1,000 km make up the synoptic-scale and smaller wavelengths the meso-scale. An example of a scale-separated wind field is shown in Figure S5 in Supporting Information S1. By computing the cross-frontal differences of the cross- and along-frontal wind speeds, the "bulk" convergence and vorticity can be further evaluated (Clark & Parker, 2020). Further, the terrain height in a 150 km radius of the front is evaluated, similarly to precipitation. This is done to evaluate the influence of the orography on precipitation intensity.

To analyze the relation of the front parameters, we first take the average of the 10 frontal points of every front object with the highest standardized precipitation values. Then the front with the highest averaged standardized precipitation within a 24 hr window is preserved while others are excluded. This reduces the dependency of consecutively detected fronts over time. Standardized precipitation is used to minimize the effects of local conditions, for example, orography, on the front selection process.

The relations of the front parameter are then analyzed using quantile regression (QR) models (Koenker, 2005). A QR model is fitted with precipitation as the predictand and the front parameters as the predictors. The conditional 50th, 90th, and 99th percentiles are then estimated within the range of the specific parameter values. To assess the strength of the modeled relation, we compute the quantile verification skill score (QVSS), quantifying the goodness-of-fit of the QR model at a specific quantile with respect to the unconditional climatology of the dependent variable (Friederichs, 2010; Koenker & Machado, 1999). Possible regional differences are captured by performing this analysis for three example regions selected based on the high frequency and fraction of extreme cold frontal precipitation: Northwestern Europe (NWEUR), Southwestern Europe (SWEUR), and Central Europe (CEUR) (Figure 1a).

Additionally, we investigate the synoptic conditions and the frontal meso-scale structure of extreme front composites. For this purpose, the top 10% hourly standardized precipitating cold fronts in DJF and JJA are used to compute two types of composites. First, the large scale event conditions of every region are averaged. This enables us to evaluate synoptic phenomena. The meso-scale structure is assessed by computing front-centered composites. To this end, the conditions within a 600 km square centered at the frontal points with the highest precipitation of each event are evaluated. These squares are further rotated into the cross-frontal direction, with the x- and y-axis representing cross- and along-frontal directions, respectively. In the final step, the cross-sections of these front-centered composites are computed.

3. Results

3.1. Front Climatology

Before showing the results of the composite and the front parameter analysis we present the cold front frequency and the fraction of extreme precipitation related to cold fronts over the study region. The frequency of detected
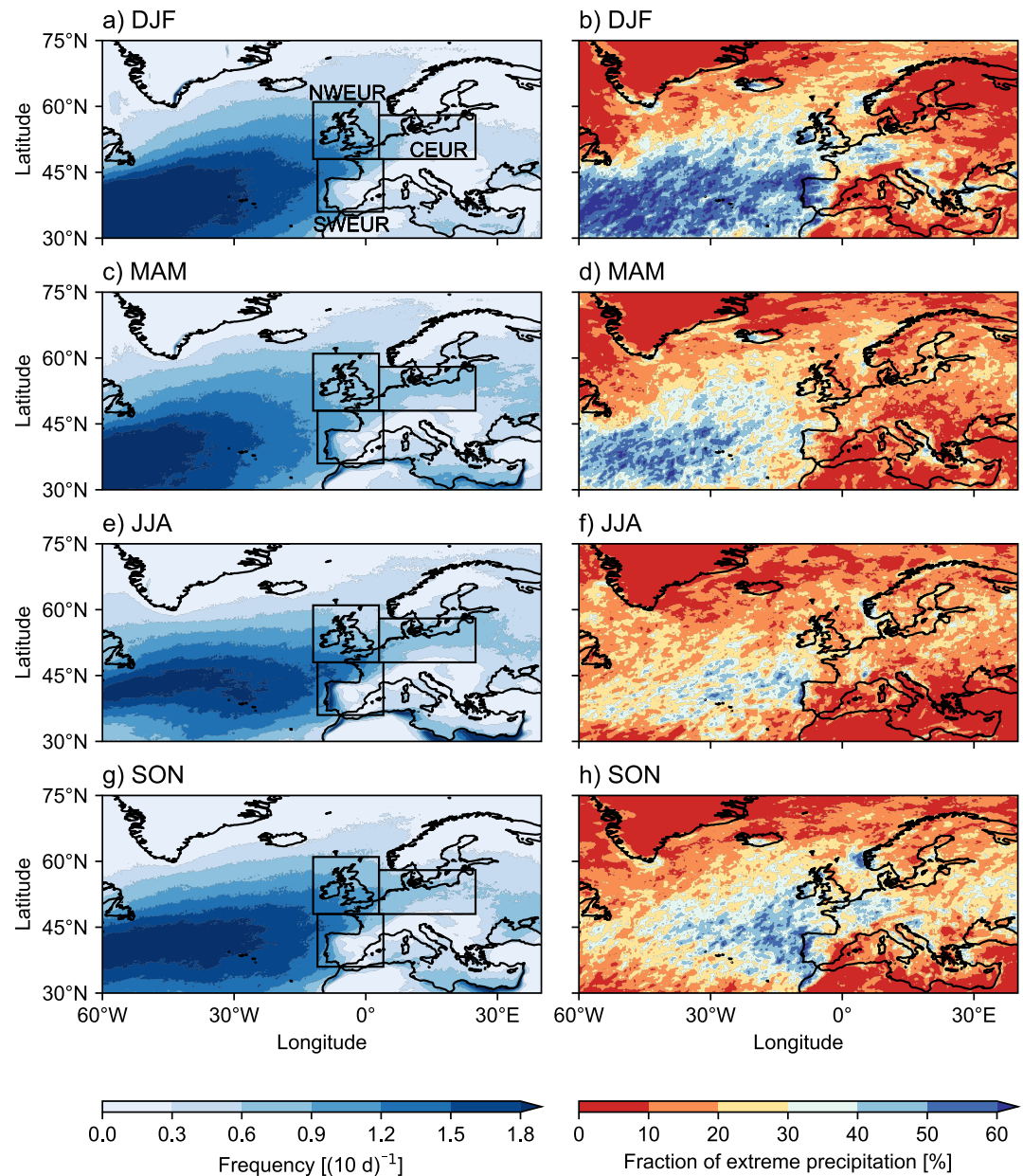
Figure 1. Cold frontal (left column) frequency per 10 days and (right column) hourly extreme precipitation fraction for (a–b) DJF, (c–d) MAM, (e–f) JJA and (g–h) SON in the period 1979–2021. We consider precipitation exceeding the 99.9th percentile of hourly precipitation as extreme. It further is classified as frontal, if it is located within a 150 km radius of a cold front point. The extent of the three analyzed regions of NWEUR (48°N–61°N, 12°E−3°W), SWEUR (36°N–48°N, 11°E−4°W) and CEUR (48°N–58°N, 3°W–25°W) is indicated.

cold fronts as well as the fraction of extreme precipitation related to cold fronts for all seasons are shown in Figure 1. The highest frequencies can be found along the storm track over the North Atlantic, dropping significantly over the continent. This can be attributed to the dissipation of $\nabla\theta_e$ due to increased friction and subsequent humidity diffusion. Cold front frequency is likely underestimated over continental Europe. Especially in DJF front objects tend to split into multiple smaller fronts which fall below the length criterion. Along the North and Baltic Sea as well as the Eastern European plains cold front frequency remains substantial. Considerable numbers are also found in the Mediterranean. Peaks at the West Iberian, North African and Levantine coasts in MAM, JJA and SON are related to strong diurnal ocean and land differences in humidity and temperature. Front frequency is
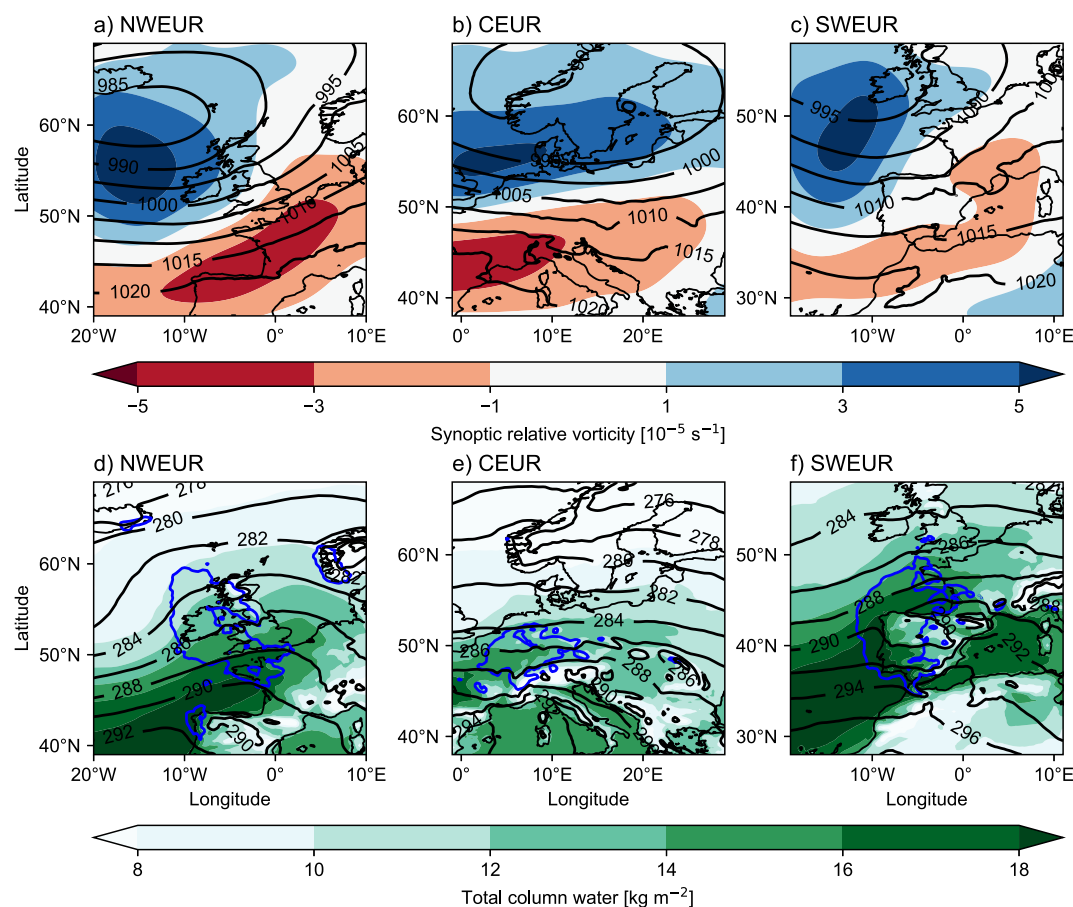
Figure 2. Synoptic composites of top 10% hourly standardized precipitating cold fronts in DJF: (a–c) black contours indicate mean sea level pressure in hPa, shading the relative synoptic vorticity at 300 hPa; (d–f) black contours θ at 850 hPa in K, blue contours areas exceeding 0.4 mm hourly precipitation, green shading the total column water vapor. Left column NWEUR, middle column CEUR, right column SWEUR.

by design relatively constant throughout the year due to the season-dependent threshold. These results are comparable to prior studies (Berry et al., 2011; Catto et al., 2014; Schemm et al., 2015).

We define extreme precipitation as hourly precipitation exceeding the 99.9th percentile for every grid point, corresponding to a 42 days return period. It is further labeled as cold frontal if a grid point classified as cold frontal is located within a 150 km radius of the precipitation. The fraction of the summed up cold frontal extreme precipitation compared to the total sum of extreme precipitation is highest over the North Atlantic (40%–80%), with peaks over western Iberia (DJF up to 70%), the British Isles (DJF and SON 50%), Central Europe (DJF and SON 50%) and Norway (SON 50%). Overall highest values are found in DJF and the lowest in JJA. In DJF, low cold frontal precipitation is found in Eastern Europe, most likely due to the aforementioned cold front underestimation.

3.2. Synoptic Conditions

The synoptic conditions are exemplified by region centered composites for DJF in the three regions in Figure 2. The JJA Figure is available in the Supporting Information S1 (Figure S6). Depending on the region and season, between 200 and 400 fronts are used for the computation of the composites.

All regions exhibit a strong westerly regime. In NWEUR the cyclone center is located between Iceland and the British Isles, in SWEUR to the west of Ireland and for CEUR over Scandinavia. Due to the slowing down of the fronts over the continent (Peng et al., 2001), the composite cyclone location in CEUR is further to the east relative to the front. The upper-level jet, depicted as the area between the cyclonic (positive) and anticyclonic (negative)

vorticity regions at 300 hPa (Figures 2a–2c), follows a north-easterly trajectory in NWEUR and SWEUR and an easterly direction in CEUR. Notably, in NWEUR and SWEUR areas of high precipitation are collocated with the left-exit region of the jet-streak, attributable to upper-level divergence and subsequent increased convection.

In NWEUR the areas of highest precipitation are to the south-east in the vicinity of the cyclone, suggesting that extremes are happening close to the occlusion point of the frontal system (Figures 2d–2f). Further, the regional precipitation patterns are markedly influenced by orography, with the windward side exhibiting the highest precipitation for example, Scottish Highlands, Alps and Iberian Plateau.

Compared to DJF, the dynamical conditions in JJA are much weaker (Figures S6a–S6c in Supporting Information S1). The position of the cyclone does not change greatly, however the pressure gradients are decreased. Although there is less dynamic forcing, there is much more moisture present in summer. Peak water content values in the warm sector are 50% higher in JJA than in DJF, especially over the continent (Figures S6d–S6f in Supporting Information S1). In CEUR and SWEUR precipitating areas shift further north-east, closer to the occlusion point. In all three regions, JJA mean cold frontal precipitation is about 25% lower than in DJF, with individual events displaying smaller affected areas with higher intensities.

3.3. Frontal Structure and Circulation

For evaluating the cross-frontal structure the same fronts as for the synoptic composite analysis are used. The frontal structure and circulation has similar patterns in all regions and seasons (DJF in Figure 3 and JJA in Figure S7 in Supporting Information S1).

The area of strongest convection is located 50–100 km ahead of the detected front (Figures 3j–3l). Here high relative humidity reaches upright to 300 hPa and subsequently slopes with the background wind (Figures 3a–3c). These high clouds, indicated by high relative humidity, can extend more than 600 km in the pre-frontal direction. Behind the top of the up-draft region there is a distinct region of subsidence, transporting low humidity stratospheric air.

Figures 3d–3l show the total across-, along-frontal and vertical wind fields, as well as the meso-scale circulation. The across-frontal circulation depicts a distinct pattern of low level convergence and high level divergence at the updraft region (Figures 3d–3f). The upper-level peak divergence height varies through the seasons, so that it reaches 500 hPa in DJF whereas in JJA it reaches 300 hPa (Figures S7d–S7f in Supporting Information S1). Starting at 800 hPa there is weak convergence sloping backwards following the frontal zone. Negative cross-frontal meso-scale circulation responsible for this, is collocated with upward motion (Figures 3j–3f). This ascending front-to-rear flow is believed to be related to symmetric instability release (Bennets & Hoskins, 1979; Schultz & Schumacher, 1999). This region further displays strong meso-scale vorticity (Figures 3g–3i). Strong vorticity is found at 50–100 km ahead of the front at 900 hPa, signifying the strength of the frontal trough.

The peak of the upper-level jet is visible at 300 hPa 50–100 km to the rear of the detected front and is oriented in the along front direction (Figures 3g–3i). The location of the low-level jet is less well defined and depends on the region and season. Its peak is around 50–300 km ahead of the front at the 900–800 hPa level and strongest in NWEUR.

As evident from the analysis of the synoptic conditions, the strength of the frontal circulation is lower in JJA than in DJF. The updraft region is narrower, more upright and exhibits lower relative humidity (Figure S7 in Supporting Information S1). The highest vertical velocity also shifts upwards from 850 to 800 hPa in DJF to 700–600 hPa in JJA. Although there is less intense circulation, peak hourly precipitation is higher in JJA than in DJF in NWEUR and CEUR. This characteristic highlights the interplay of atmospheric moisture content and dynamical forcing for cold frontal precipitation.

3.4. Quantifying the Impact of Frontal Conditions on Precipitation

From the QR analysis several key relationships between the frontal conditions and precipitation are found, that can be related to physical processes. The QR for some critical parameters are showcased in Figure 4 for DJF. To provide an initial assessment of the strength of the relationships, the QVSS of the 50th, 90th and 99th percentile QR of the combined regional and seasonal data is given in parentheses in the following paragraph (Table S11 in Supporting Information S1). Only the QVSS of the evaluation location of every parameter with the highest score
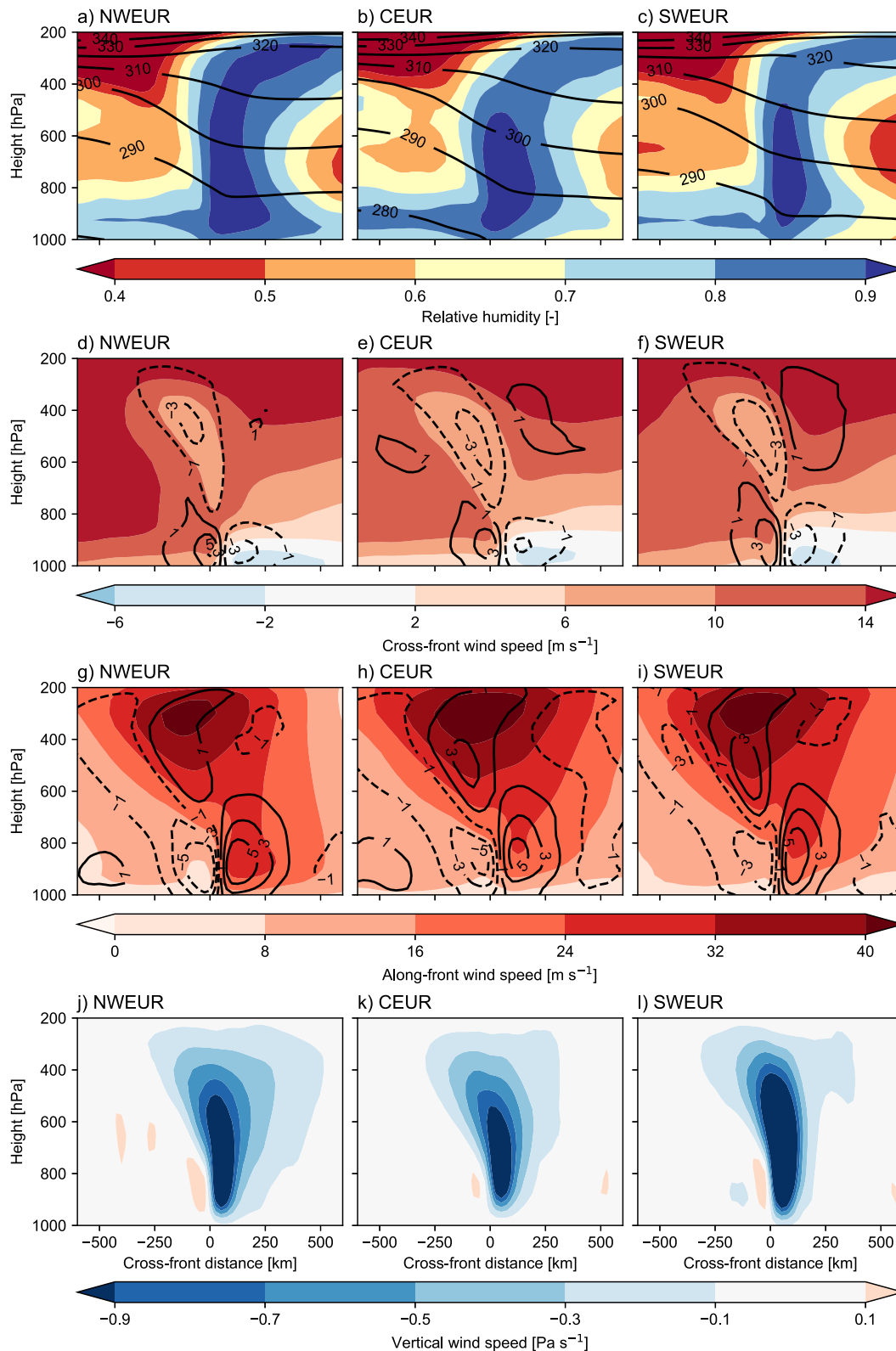
Figure 3. Front centered composite cross-sections of top 10% standardized precipitating cold fronts in DJF: (a–c) black contours indicate θ in K, shading the relative humidity; (d–f) black contours the meso-scale cross-frontal wind in m·s^{-1}, shading the total cross-frontal wind; (g–i) black contours the meso-scale along-frontal wind in m·s^{-1}, shading the total along-frontal wind (positive values point toward the cyclone center); (j–k) the vertical wind speed in Pa·s^{-1} (negative values indicate upward movement). Left column NWEUR, middle column CEUR, right column SWEUR.

are given. A comprehensive list of the regional and seasonal results is provided in the Supporting Information S1 (Tables S8–S11). All presented relationships are statistically highly significant (*t*- test *p*-value < 0.001).

Humidity at the front detection point exerts a robust positive impact across all regions and seasons (5%, 11%, 16%) (Figures 4a–4c). As can be seen by the higher QVSS and the stronger slope of the QR, extremes are more strongly affected by an increase in humidity than average fronts, most likely due to dynamical feedback processes. Interestingly, post-frontal humidity (11%, 15%, 19%) exhibits higher scores than pre-frontal humidity (2%, 8%, 14%). This effect is present through all regions and seasons. It is more likely that this is an effect of the identification of the front position, rather than of a physical process. Humidity behind (100 km) and ahead (100 km) of the front are correlated (correlation coefficient: 69%), even though within the frontal zone there is a strong change in humidity. This is also characterized by the absence of a link between specific humidity gradient and precipitation (2%, 0%, 0%).

Pre-frontal Temperature displays a strong positive impact for the higher percentiles (0%, 5%, 11%). This relation is especially strong in DJF (5%, 15%, 23%). The post-frontal temperature shows a weaker impact (1%, 2%, 6%). According to the Clausius-Clapeyron relation and the saturated condition of the warm air side of precipitating fronts, temperature strongly controls the moisture content. On the cold side of a front, there is commonly no saturation, making the temperature less of a constraint for moisture content. Additionally, latent heat release due to cloud formation in the pre-frontal sector increases the warm area temperature more strongly. This effect can also be observed in the weak positive impact of $\nabla\theta$ (4%, 3%, 2%). Furthermore, $\nabla\theta$ has some positive relation with meso-scale convergence (2%, 5%, 8% (Table S12 in Supporting Information S1)) and meso-scale vorticity (4%, 8%, 9% (Table S13 in Supporting Information S1)). This may be due to the relation of ageostrophic circulation and $\nabla\theta$ in a frontal system (Eliassen, 1962; Sawyer, 1956).

Meso-scale convergence exhibits a strong positive link with precipitation (9%, 13%, 17%) (Figures 4d–4f). Similarly, the synoptic cross-frontal convergence has a positive impact (8%, 8%, 7%). These results can be attributed to the impact of convergence on convection, as well as transport of humidity into the updraft region.

The synoptic along-front wind speed in the pre-frontal sector, quantifying the warm conveyor belt velocity, has a strong positive impact (18%, 12%, 8%) (Figures 4g–4i). The relation is especially strong in DJF in NWEUR (25%, 19%, 13% (Table S8 in Supporting Information S1)) and SWEUR (28%, 30%, 22% (Table S10 in Supporting Information S1)). Higher values may be related to stronger cyclones and higher moisture transport toward the front.

Synoptic vorticity has a strong positive impact (11%, 6%, 5%). This effect is especially strong in NWEUR (16%, 12%, 9% (Table S8 in Supporting Information S1)), most likely due to the common occurrence of frontal waves and secondary cyclogenesis in this region (Priestley et al., 2020; Rivals et al., 1998). Meso-scale vorticity also shows a strong positive relationship in all regions and seasons (21%, 17%, 13%), especially in SON (25%, 22%, 17%) (Figures 4j–4l). The reason is likely to be that strong front relative vorticity is due to a strong frontal trough, which is related to updrafts and latent heat release above the surface front (Clark & Parker, 2020).

In general more variance can be explained in DJF than in JJA, with SON and MAM in between. This could be due to higher moist static energy and subsequent possible instability release in warmer seasons which is not quantified by the front parameters. Regional differences are also identified. In NWEUR and SWEUR synoptic processes have a strong impact, whilst meso-scale processes show high scores in CEUR and SWEUR, potentially due to increased frictional processes over orographic features.

4. Conclusion

In this study we evaluate the conditions of objectively detected cold fronts in ERA5 reanalysis data. In Europe some regions with high cold front frequency are found. The associated precipitation in these areas amounts up to 70% of all extreme precipitation, particularly in DJF and SON.

Analyzing these regions in detail, a strong westerly flow regime, high moisture content in the warm conveyor belt and upper-level divergence in the jet-streak region coincide with cold frontal extreme precipitation events in all regions.
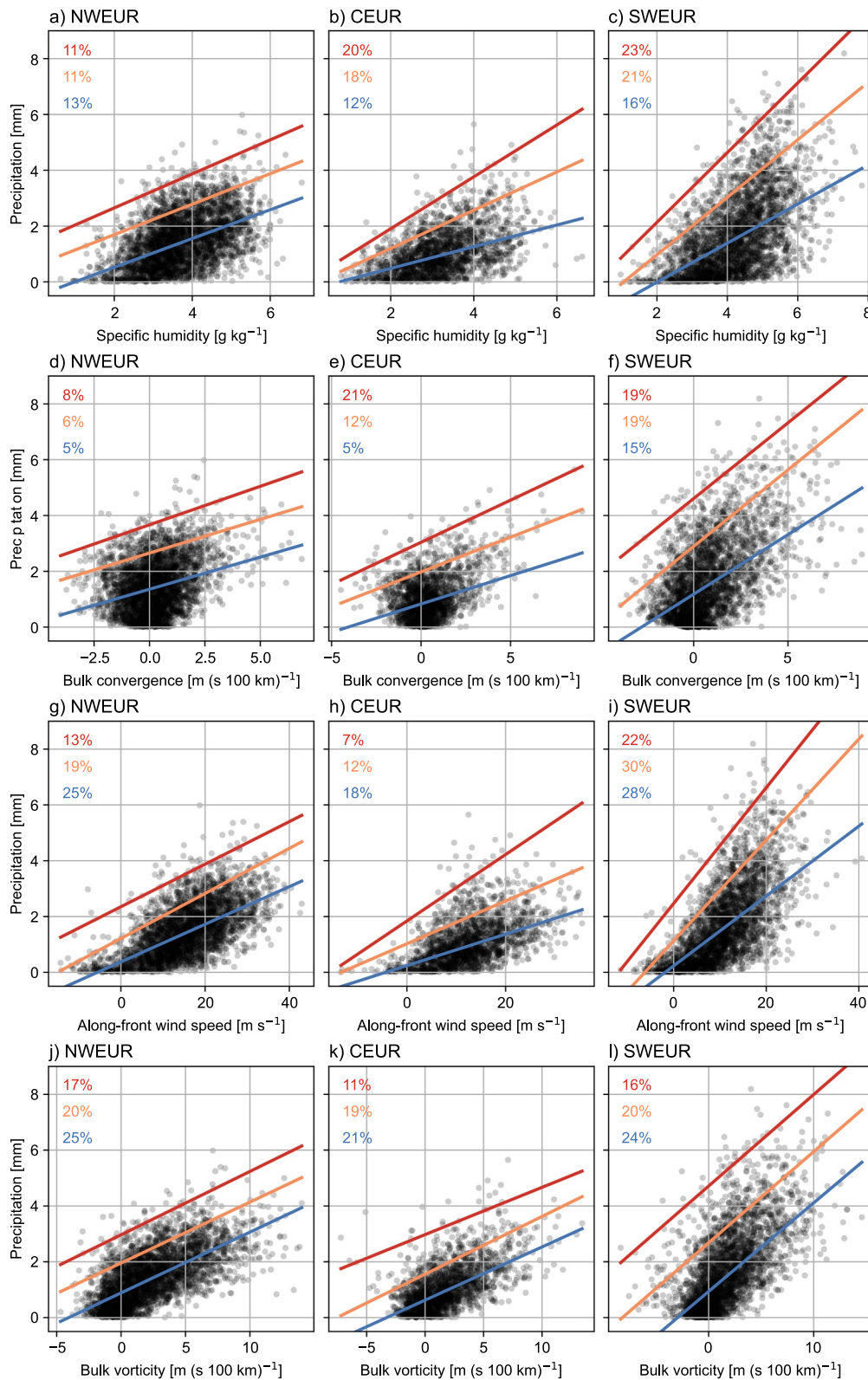
Figure 4. DJF relation of precipitation and (a–c) specific humidity at the location of the front, (d–f) meso-scale bulk convergence, (g–i) 300 km pre-frontal synoptic along-front wind speed, (j–l) meso-scale bulk vorticity. Left column NWEUR, middle column CEUR, right column SWEUR. The colored lines indicate the (blue) 50th, (orange) 90th and (red) 99th percentile of the QR model. The percentages in the corresponding colors indicate the QVSS. The black dots indicate the frontal data points.

The front relative circulation patterns are also similar in all regions and seasons and agree well with frontal dynamic theory. In DJF dynamic forcing is stronger than in JJA, however higher atmospheric moisture content affects cold frontal precipitation strongly, making JJA rates higher in some regions.

We find a key role of moisture content and synoptic moisture transport, as well as the strength of the meso-scale circulation as drivers of frontal precipitation. However, our analysis cannot identify whether the conditions are the cause or the result of strong convection and latent heat release at the frontal zone. Furthermore, ERA5 does not resolve all relevant processes and is too coarse to represent the highest precipitation values in a narrow cold frontal precipitation band.

These results can serve as the basis for model evaluation, to study the biases and added value across a hierarchy of climate models. Additionally, applying this analysis to future climate simulations may provide a physical explanation of changes in frontal extreme precipitation and therefore increases trust in projections.

Data Availability Statement

The ECMWF reanalysis ERA5 dataset is available at Hersbach et al. (2020). The front detection algorithm and the code used for probing the front parameter is available at https://wegcgitlab.uni-graz.at/ars/INTERACT_code.

References

Bennets, D., & Hoskins, B. (1979). Conditional symmetric instability – A possible explanation for frontal rainbands. *The Quarterly Journal of the Royal Meteorological Society*, *105*(446), 945–962. https://doi.org/10.1256/smsqj.44614

Berry, G., Jakob, C., & Reeder, M. (2011). Recent global trends in atmospheric fronts: Global trends in atmospheric fronts. *Geophysical Research Letters*, *38*(21), n/a–n/a. Retrieved 2021-12-10, from https://doi.org/10.1029/2011GL049481

Catto, J. L., Jakob, C., Berry, G., & Nicholls, N. (2012). Relating global precipitation to atmospheric fronts. *Geophysical Research Letters*, *39*(10), 2012GL051736. Retrieved 2024-01-22, from https://doi.org/10.1029/2012GL051736

Catto, J. L., Madonna, E., Joos, H., Rudeva, I., & Simmonds, I. (2015). Global relationship between fronts and warm conveyor belts and the impact on extreme precipitation. *Journal of Climate*, *28*(21), 8411–8429. Retrieved 2021-12-10, from. https://doi.org/10.1175/JCLI-D-15-0171.1

Catto, J. L., Nicholls, N., Jakob, C., & Shelton, K. L. (2014). Atmospheric fronts in current and future climates. *Geophysical Research Letters*, *41*(21), 7642–7650. Retrieved 2021-12-10, from https://doi.org/10.1002/2014GL061943

Catto, J. L., & Pfahl, S. (2013). The importance of fronts for extreme precipitation: Fronts and precipitation extremes. *Journal of Geophysical Research: Atmospheres*, *118*(19), 10791–10801. Retrieved 2021-12-10, from https://doi.org/10.1002/jgrd.50852

Catto, J. L., & Raveh-Rubin, S. (2019). Climatology and dynamics of the link between dry intrusions and cold fronts during winter. Part I: Global climatology. *Climate Dynamics*, *53*(3–4), 1873–1892. Retrieved 2023-07-17, from https://doi.org/10.1007/s00382-019-04745-w

Clark, M. R., & Parker, D. J. (2020). Synoptic-scale and mesoscale controls for tornadogenesis on cold fronts: A generalised measure of tornado risk and identification of synoptic types. *Quarterly Journal of the Royal Meteorological Society*, *146*(733), 4195–4225. Retrieved 2023-07-05, from. https://doi.org/10.1002/qj.3898

Collins, M., Minobe, S., Barreiro, M., Bordoni, S., Kaspi, Y., Kuwano-Yoshida, A., et al. (2018). Challenges and opportunities for improved understanding of regional climate dynamics. *Nature Climate Change*, *8*(2), 101–108. Retrieved 2021-12-10, from. https://doi.org/10.1038/s41558-017-0059-8

Denis, B., Côté, J., & Laprise, R. (2002). Spectral decomposition of two-dimensional atmospheric fields on limited-area domains using the discrete cosine transform (DCT). *Monthly Weather Review*, *130*(7), 1812–1829. Retrieved 2021-12-10, from https://doi.org/10.1175/1520-0493(2002)130⟨1812:SDOTDA⟩2.0.CO;2

Eliassen, A. (1962). On the vertical circulation in frontal zones. *Geofysiske Publikasjoner*, *24*(4), 147–160.

Feser, F., & von Storch, H. (2005). A spatial two-dimensional discrete filter for limited-area-model evaluation purposes. *Monthly Weather Review*, *133*(6), 1774–1786. Retrieved 2023-07-05, from https://doi.org/10.1175/MWR2939.1

Friederichs, P. (2010). Statistical downscaling of extreme precipitation events using extreme value theory. *Extremes*, *13*(2), 109–132. Retrieved 2023-07-19, from https://doi.org/10.1007/s10687-010-0107-5

Hénin, R., Ramos, A. M., Schemm, S., Gouveia, C. M., & Liberato, M. L. R. (2019). Assigning precipitation to mid-latitudes fronts on sub-daily scales in the North Atlantic and European sector: Climatology and trends. *International Journal of Climatology*, *39*(1), 317–330. Retrieved 2021-12-10, from https://doi.org/10.1002/joc.5808

Hersbach, H., Bell, B., Berrisford, P., Hirahara, S., Horányi, A., Muñoz-Sabater, J., et al. (2020). The ERA5 global reanalysis. *Quarterly Journal of the Royal Meteorological Society*, *146*(730), 1999–2049. Retrieved 2023-07-17, from. https://doi.org/10.1002/qj.3803

Hewson, T. D. (1998). Objective fronts. *Meteorological Applications*, *5*(1), 37–65. Retrieved 2021-12-10, from https://doi.org/10.1017/S1350482798000553

Hoskins, B., & James, I. N. (2014). *Fluid dynamics of the midlatitude atmosphere*. Wiley Blackwell.

Houze, R. A., & Hobbs, P. V. (1982). Organization and structure of precipitating cloud systems. In *Advances in geophysics* (Vol. 24), 225–315. Elsevier. Retrieved 2024-03-07, from https://doi.org/10.1016/S0065-2687(08)60521-X

Jenkner, J., Sprenger, M., Schwenk, I., Schwierz, C., Dierer, S., & Leuenberger, D. (2009). Detection and climatology of fronts in a high-resolution model reanalysis over the Alps. *Meteorological Applications*, *17*, (1), 1. n/a–n/a. 18, Retrieved 2021-12-10, from https://doi.org/10.1002/met.142

Koenker, R. (2005). *Quantile regression*. Cambridge University Press. Retrieved 2024-01-05, from. https://doi.org/10.1017/CBO9780511754098

Koenker, R., & Machado, J. A. F. (1999). Goodness of fit and related inference processes for quantile regression. *Journal of the American Statistical Association*, *94*(448), 1296–1310. Retrieved 2023-07-19, from https://doi.org/10.1080/01621459.1999.10473882

Lin, Y.-L. (2007). *Mesoscale dynamics*. Cambridge University Press. Retrieved 2021-12-10, from https://doi.org/10.1017/CBO9780511619649

Marotzke, J., Jakob, C., Bony, S., Dirmeyer, P. A., O'Gorman, P. A., Hawkins, E., et al. (2017). Climate research must sharpen its view. *Nature Climate Change*, *7*(2), 89–91. Retrieved 2021-12-10, from https://doi.org/10.1038/nclimate3206

Peng, M. S., Powell, J. H., Williams, R. T., & Jeng, B.-F. (2001). Boundary layer effects on fronts over topography. *Journal of the Atmospheric Sciences*, *58*(15), 2222–2239. Retrieved 2024-08-14, from https://doi.org/10.1175/1520-0469(2001)058⟨2222:BLEOFO⟩2.0.CO;2

Priestley, M. D. K., Dacre, H. F., Shaffrey, L. C., Schemm, S., & Pinto, J. G. (2020). The role of secondary cyclones and cyclone families for the North Atlantic storm track and clustering over western Europe. *Quarterly Journal of the Royal Meteorological Society*, *146*(728), 1184–1205. Retrieved 2024-02-08, from https://doi.org/10.1002/qj.3733

Raveh-Rubin, S., & Catto, J. L. (2019). Climatology and dynamics of the link between dry intrusions and cold fronts during winter, Part II: Front-centred perspective. *Climate Dynamics*, *53*(3–4), 1893–1909. Retrieved 2023-07-17, from https://doi.org/10.1007/s00382-019-04793-2

Renard, R. J., & Clarke, L. C. (1965). Experiments in numerical objective frontal analysis[1]. *Monthly Weather Review*, *93*(9), 547–556. Retrieved 2023-07-17, from https://doi.org/10.1175/1520-0493(1965)093⟨0547:EINOFA⟩2.3.CO;2

Ritter, R. (2014). A novel front detection algorithm tested in complex terrain. Retrieved 2021-12-10, from http://wegcwww.uni-graz.at/publ/wegcreports/2014/WCV-SciRep-No60-RRitter-Sep2014.pdf. (OCLC: 1073806003).

Rivals, H., Cammas, J., & Renfrew, I. A. (1998). Secondary cyclogenesis: The initiation phase of a frontal wave observed over the eastern Atlantic. *Quarterly Journal of the Royal Meteorological Society*, *124*(545), 243–267. Retrieved 2024-02-28, from https://doi.org/10.1002/qj.49712454511

Rüdisühli, S., Sprenger, M., Leutwyler, D., Schär, C., & Wernli, H. (2020). Attribution of precipitation to cyclones and fronts over Europe in a kilometer-scale regional climate simulation. *Weather and Climate Dynamics*, *1*(2), 675–699. Retrieved 2021-12-10, from https://doi.org/10.5194/wcd-1-675-2020

Sawyer, J. S. (1956). The vertical circulation at meteorological fronts and its relation to frontogenesis. *Proceedings of the Royal Society of London, Series A: Mathematical and Physical Sciences*, *234*(1198), 346–362. Retrieved 2023-07-17, from https://doi.org/10.1098/rspa.1956.0039

Schemm, S., Rudeva, I., & Simmonds, I. (2015). Extratropical fronts in the lower troposphere-global perspectives obtained from two automated methods: Fronts in the Lower Troposphere. *Quarterly Journal of the Royal Meteorological Society*, *141*(690), 1686–1698. Retrieved 2021-12-10, from https://doi.org/10.1002/qj.2471

Schemm, S., Sprenger, M., Martius, O., Wernli, H., & Zimmer, M. (2017). Increase in the number of extremely strong fronts over Europe? A study based on ERA-interim reanalysis (1979–2014): Extremely strong fronts over Europe. *Geophysical Research Letters*, *44*(1), 553–561. Retrieved 2021-12-10, from https://doi.org/10.1002/2016GL071451

Schultz, D. M., & Schumacher, P. N. (1999). The use and misuse of conditional symmetric instability. *Monthly Weather Review*, *127*(12), 2709–2732. Retrieved 2024-02-16, from https://doi.org/10.1175/1520-0493(1999)127⟨2709:TUAMOC⟩2.0.CO;2